

# Wavelet analysis of millisecond variability of Cygnus X-1 during its failed state transition

Paweł Lachowicz<sup>1\*</sup> and Bożena Czerny<sup>1</sup>

<sup>1</sup>*Nicolaus Copernicus Astronomical Center, Bartycka 18, 00-716 Warszawa, Poland*

arXiv:astro-ph/0412136v1 6 Dec 2004

23 May 2019

## ABSTRACT

Application of multi-resolution analysis adopting wavelets in order to investigate millisecond aperiodic X-ray variability of Cyg X-1 is presented. This relatively new approach in time-series analysis allows us to study both the significance of any localized in time–frequency space flux oscillation as well as the stability of its period. Using the observations of the *RXTE/PCA* we analyze archival data from Cyg X-1 during its failed state transition. The power spectrum of such a state is strongly dominated by a single Lorentzian peak corresponding to a dumped oscillator. Our wavelet analysis presented in this paper shows the existence of short lasting oscillations without obvious trend in the frequency domain. Based on this result, we suggest the interpretation of the dominant components of Cyg X-1 power spectrum in all spectral states: (i) power law component dominating soft state is due to accretion rate fluctuations related to MRI instability in the cold disk, (ii) the low frequency Lorentzian is related to the same fluctuations but in the inner ion torus, and (iii) the high frequency Lorentzian (dominating the power spectrum during the failed state transition) is due to the dynamical pulsations of the inner ion torus.

The usage of wavelet analysis as a potential and attractive tool in order to search and trace *semi-direct* evidences of accretion process onto black-hole is proposed.

**Key words:** accretion, accretion disks – binaries: general – stars: individual: Cyg X-1 – X-rays: observations – X-rays: stars.

## 1 INTRODUCTION

Cyg X-1 (Bowyer et al. 1965) belongs to the class of Galactic accreting black-hole binaries characterized by highly variable X-ray emission on time-scales covering up to ten orders of magnitude (e.g. Nowak et al. 1999; Reig, Papadakis & Kylafis 2002; Psaltis 2004). Optical companion, HDE 226868 star (Bolton 1972; Webster & Murdin 1972) was classified as O9.7Iab supergiant (Walborn 1973) with orbital period of 5.6 d. The main source of matter accreting onto black hole is focused stellar wind taking its origin from HDE 226868. Mass ranges of components are 10–32 M<sub>⊙</sub> and 16–55 M<sub>⊙</sub> for black-hole and supergiant, respectively (Gies & Bolton 1986; Herrero et al. 1995; Ziolkowski 2004).

The power spectrum density (PSD) of the X-ray emission is broad-band and aperiodic. It was frequently characterized as a broken power-law (Sutherland, Weiskopf & Kahn 1978; Belloni & Hasinger 1990; Nowak et al. 1999; Revnivtsev, Gilfanov & Churazov 2000), with occasional narrow quasi-periodic features (QPO) (Angelini, White &

Stella 1992). Higher quality data allowed for more sophisticated parameterization of the PSD through a number of broad Lorentzians and a power-law component (e.g. Nowak 2000; Pottschmidt et al. 2003, hereafter P03). The lightcurve is not stationary. In short time-scales the variance is proportional to the mean luminosity of the source (Uttley & McHardy 2001; Gleissner et al. 2004) so the normalized power spectrum is broadly used to characterize the source (Miyamoto et al. 1992 and most subsequent papers). In long time-scales also the shape of the PSD changes as it depends significantly on the spectral state of the source (e.g. Cui et al. 1997a; 1997b).

Although frequently used, Fourier-based technique is actually not suitable for the analysis of the aperiodic variability. Fourier analysis uses a fixed sinusoidal basis functions as a model to decompose a signal. This method therefore provides excellent frequency resolution of persistent features but it fails when the signal is highly aperiodic and existing modulations are needed to be localized in time–frequency space.

To overcome this problem one needs to use multi-resolution approach, e.g. by wavelet analysis (WA). Because

\* E-mail: paulo@camk.edu.pl

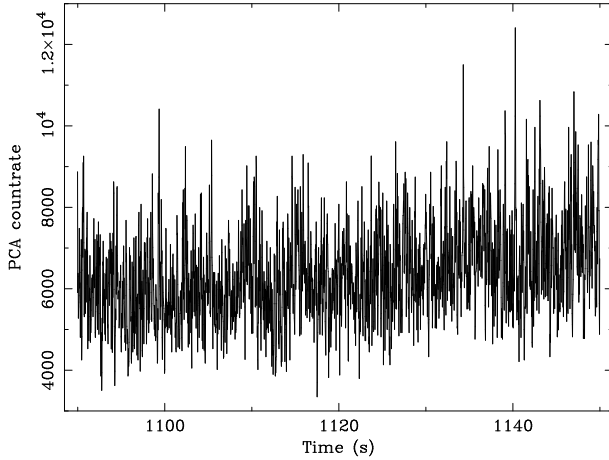


**Figure 1.** The lightcurve of Cyg X-1 as observed by the *RXTE*/PCA on 1999.12.05, showing a 60 s sequence of data selected by us for deeper studies using wavelet analysis.

wavelet decomposition gives an idea of both the local frequency content of a time-series and the temporal distribution of these frequencies, its application in astronomical signal processing is increasing rapidly (e.g. Szatmary, Vinko & Gal 1994; Escalera & MacGillivray 1995; Frick et al. 1997; Aschwanden et al. 1998; Barreiro & Hobson 2001; Freeman et al. 2002; Irastorza et al. 2003; Garcia-Lorenzo et al. 2004). Interestingly, so far the application of wavelets in order to study variability of X-ray binary systems and active galactic nuclei was marginal. Scargle et al. (1993) used them to examine QPO and very low-frequency noise for Sco X-1 whereas Steiman-Cameron et al. (1997) supplemented Fourier detection of quasi-periodic oscillations in optical lightcurves of GX 339-4 by scalograms, a wavelet technique. Fritz & Bruch (1998) applied this technique to the analysis of the optical luminosity variations in cataclysmic variables while Liszka, Pacholczyk & Stoeger (2000a) analyzed the ROSAT lightcurve of NGC 5548 in short time-scales.

In this paper we select a very special observation of Cyg X-1 performed on 1999.12.05. It was examined by P03 and the state of the source was described as failed state transition. The power spectrum at that time was particularly simple since the dominant part of the power was contained in a single Lorentzian peak. The aim of our paper is to verify with the wavelet analysis whether indeed a simple damped oscillator well represents the time-resolved lightcurve properties.

Our paper is organized as follows. Section 2 provides information on our data selection and reduction. In Section 3 we describe most essential aspects of the time-frequency analysis, starting from a brief discussion of computing X-ray power spectra and associated time-resolution problem. Next, we provide a description of calculation of continuous wavelet transform in the frame of our interest. Section 4 contains the analysis of Cyg X-1 lightcurve whereas a discussion of results, including lightcurve simulations, is the subject of Section 5. We conclude in Section 6.

## 2 DATA SELECTION AND REDUCTION

To probe the object variability on time-scales of seconds we use the observation by Proportional Counter Array on board of the *Rossi X-ray Timing Explorer* (*RXTE*/PCA; Bradt, Rothschild & Swank 1993) taken from the public archive of the HEASARC. We select the PCA data set of 40099-01-24-01 (1999.12.05) on which we concentrate our investigation. The data were reduced with the LHEASOFT package v. 5.3.1 (May 2004) applying a standard data selection, i.e. the Earth elevation angle  $> 10^\circ$ , pointing offset  $< 0^\circ.01$ , the time since the peak of the last South Atlantic Anomaly SAA  $> 30$  min and the electron contamination  $< 0.1$ . The number of Proportional Counting Units (PCUs) opened during an observation was equal 3.

We extract the lightcurve in 2.03–13.1 keV energy band (channels 0–30) and rebin it with one common bin size value of  $\Delta t = 0.025$  s. The average count-rate in this set is  $\bar{x} = 6061.8 \text{ cts s}^{-1}$  and the fractional rms 21.6 %. For needs of computation of Fourier power spectra, we use POWSPEC software with applied Poisson noise level subtraction. For purposes of wavelet analysis, the IDL software provided by Torrence & Compo (1998) (hereafter TC98; see Acknowledgments for the URL address) was run.

## 3 TIME-FREQUENCY ANALYSIS

### 3.1 Fourier power spectrum and time-resolution problem

Computation of Fourier power spectral density (PSD),  $\mathcal{P}(\nu)$ , is an ideal tool for detecting periodic fluctuations in time series. Therefore, in the absence of major problems caused by window pattern (aliasing) and at high signal-to-noise ratio, a strong peak in the Fourier spectrum has an immediate interpretation (e.g. Gray 1976).

The continuous  $\mathcal{P}(\nu)$  is representative of the true, underlying process  $x(t)$ :

$$\mathcal{P}(\nu) = \left| \int_{-\infty}^{\infty} x(t) e^{-i2\pi\nu t} dt \right|^2, \quad (1)$$

whereas its best discrete estimator,  $P(\nu)$ , is a periodogram. In X-ray astronomy, well established method for the power spectrum calculation of discretely and unevenly distributed data is the Lomb-Scargle periodogram (Lomb 1976; Scargle 1982; see also Press et al. 1992 for summary). Its form simplifies when one needs to deal with equally spaced observations and a lightcurve is spread continuously (without gaps). In such case, periodogram can be defined as follows:

$$P_j = A |\hat{x}_j|^2 - P_{\text{noise}}, \quad (2)$$

where  $A$  represents normalization factor to the units of interest and  $P_{\text{noise}}$  a level of white noise to be subtracted (see below). The Fourier amplitude,  $\hat{x}_j$ , takes form:

$$\hat{x}_j = N_{\text{obs}}^{-1} \sum_{k=0}^{N_{\text{obs}}-1} (x_k - \bar{x}) e^{-i2\pi j k / N_{\text{obs}}} \quad (3)$$

where  $x(t) \equiv x(t_k) \equiv x_k$  is the flux value in the time interval  $(x_k, x_k + \Delta t)$ ;  $t_k = k\Delta t$ ,  $k = 0, \dots, N_{\text{obs}} - 1$ ;  $N_{\text{obs}}$  is the total number of data points in a lightcurve;  $\Delta t$  is a bin time (and the sampling resolution of a lightcurve as well)

where  $T = N_{\text{obs}}\Delta t$  denotes the total time span of data. A subtraction of the average flux,  $(x_k - \bar{x})$ , is applied to avoid great power of a signal at zero frequency during calculation of the Fourier transform. A relation between  $j$  and frequency  $\nu$  is described as  $\nu = j/T = j/(N_{\text{obs}}\Delta t)$  where  $j = 1, 2, \dots, N_{\text{obs}}/2$ . Because of a time limitation of a time-series, the underlying process  $x(t)$ , originally spanned for  $-\infty < t < \infty$ , is bounded by an observing window  $w(t)$ , such that  $x(t)w(t)$  equals  $x(t)$  for  $k = 0, \dots, N_{\text{obs}} - 1$  and zero elsewhere, where  $t_0$  and  $t_{N_{\text{obs}}-1}$  denotes the time of the first and the last observation, respectively. Therefore, the overall periodogram can be calculated for a given interval of frequencies with a frequency step equal to  $\Delta\nu = T^{-1}$ , limited by  $T^{-1}$  and the Nyquist frequency  $(2\Delta t)^{-1}$  in the low- and high-frequency region, respectively.

Most commonly used normalization of X-ray power spectral densities follows the one used by Miyamoto et al. (1992) and defined as:

$$A = 2\Delta t N_{\text{obs}} \bar{x}^{-2} \quad (4)$$

which gives the periodogram (2) normalized to the units of square fractional root-mean-square (rms) per frequency interval, i.e.  $(\text{rms}/\text{mean})^2/\text{Hz}$ . Therefore, integrated periodogram yields the square of fractional rms of a lightcurve. Because PSD normalized with (4) is count-rate independent, it allows to compare the shapes of Fourier power spectra from different objects which observations may also come from different detectors (van der Klis 1989; 1997). Please note that formula (4) is valid assuming flux  $x_k$  to be in units of counts per second.

The counting method applied in the X-ray flux measurements is associated with the presence of a certain noise level. It results in a lightcurve as the Poisson noise having significant contribution to the power (of power spectrum) at all frequencies. Its value is constant and should to be subtracted from the PSD. For a binned lightcurve evenly distributed over time, in the absence of side effects (e.g. caused by dead-time of detector; see Zhang et al. 1995) and at assumed level of the mean background count-rate equal zero, the expected Poisson noise level equals  $P_{\text{noise}} = 2/\bar{x}$  (see Vaughan et al. 2003 for review). This is applicable for purposes of the PCA data we deal with within this project.

An application of periodogram in order to estimate best  $\mathcal{P}(\nu)$  involves a projection of observations  $x(t)$  onto a fixed model basis  $x(t)_{\parallel}$ . In case of discrete Fourier transform the basis is represented by the sine and cosine functions,  $x(t)_{\parallel} \equiv e^{-i2\pi\nu t}$ , which are symmetric and unlimited in time. A value of  $P_j$  provides an information on the consistency between data and a model in a function of frequency. The square of Fourier amplitude,  $|\hat{x}_j|^2$ , reaches the top values at frequencies corresponding to sinusoidal modulations concealed in a lightcurve. However, such representation of power loses its significance in case when analyzed lightcurve reflects aperiodic broad-band variabilities rather than periodic ones. Thus, the square of  $\hat{x}_j$  returns only a partial information about true value of variability due to poor consistency of data with a sinusoidal model.

Fourier analysis fails when time evolution of spectral features has to be taken into account. In practice, there is a weak probability of solid stationary condition to be preserved for each of detected modulations. An amplitude and/or phase may fluctuate slightly and locally in time. This

is impossible to detect performing solely a computation of Fourier periodogram. In order to capture all such features one needs to apply time-frequency representation of the signal. One solution to this problem is the application of Windowed Fourier Transform (WFT). An idea is to chop up a lightcurve into short intervals and analyze them separately for their frequency content. Thus, we are interested in studying properties of time-series at time  $t$ , suppressing the signal at other times. One can achieve it by multiplication of the lightcurve  $x(t)$  with a finite observing window,  $u(t)$ , centered at  $t$ , producing a modified signal  $x_m(\tau)$  as a function of fixed time of  $t$  and running time of  $\tau$  as follows:

$$x_m(\tau) = x(\tau)u(\tau - t). \quad (5)$$

Therefore, a square of the Windowed Fourier Transform amplitude<sup>1</sup>,  $W(\tau, \nu)$ , takes form:

$$|W(t, \nu)|^2 = \left| \int x(\tau)u^*(\tau - t)e^{i2\pi\tau\nu} d\tau \right|^2 \quad (6)$$

where  $*$  denotes complex conjugate (e.g. Flandrin 1999). A proper choice of  $u(\tau)$  is to leave the signal more or less unaltered around the time  $t$  but to suppress it for times distant enough from the time of interest (Cohen 1995). Transformation  $W(\tau, \nu)$  can serve as a representation of underlying physical processes in a function of time and frequency, making a compromise between studies in both domains.

Unfortunately, WFT suffers from at least three main problems. First one refers to a fixed width of an observing window limited by our choice at hand (resolution problem). Making the window narrower we force a loss of frequency information. Second problem regards the Heisenberg Uncertainty Principle. Originally applied to the momentum and location of moving particles has a strict transformation into time-series analysis. According to it, one cannot know the exact time-frequency representation of the signal. Instead, what one can know are rather time intervals in which certain band of frequencies exist. Finally, the last aspect corresponds to the fact that WFT maintains a constant frequency resolution limited by a window's width. Therefore, it provides no opportunity in finding any of other finer flux fluctuation of width enough small to be resolved by locally calculated WFT.

### 3.2 Wavelet analysis

To cope with all these problems one needs to apply an alternative approach in the form of multi-resolution analysis. A basic concept standing for its application to time-series was to analyze the signal at different frequencies with different resolutions. It gave a cornerstone to the wavelet analysis. Contrary to Fourier transform, wavelet analysis makes use of a set of functions, *wavelets*, which are localized in scale-time space<sup>2</sup>. Wavelets represent mathematical functions of finite length, characterized, in general, by symmetric or asymmetric damping profile at both sides. The crucial idea of

<sup>1</sup> Also known under the name of *dynamical power spectrum*, *spectrogram* or *dynamical periodogram* (see e.g. Wilms et al. 2001 for such time-frequency representation for LMC X-3).

<sup>2</sup> In wavelet analysis a term *scale* is used instead of *frequency* which is reserved for the Fourier analysis.

WA is to search for structures appearing locally within a lightcurve, which may resemble *scaled* and *time-shifted* version of original wavelet function, here also called as *mother wavelet*. A time-series can be represented in terms of wavelet expansion, i.e. as superposition of elementary functions of known scale and time location. For a given wavelet basis, wavelet transform works in order to search for amplitudes of local fluctuations obtained from projecting a lightcurve onto this basis. Because of scaling and time-shifting properties of mother wavelet, wavelet transform can be considered as WFT with varying window's width which, conversely to WFT, depends on frequency. Therefore, it makes a huge advantage of wavelets for studying time-dependent phenomena (i.e. transient signals, sharp peaks, quasi-periodic oscillations) of different duration and shape occurring at different frequencies.

Below we give a short review on fundamentals of application of wavelets into time-series analysis after Farge (1992), Daubechies (1992) and TC98.

### 3.2.1 Wavelets

Consider a mother wavelet function,  $\psi(t)$ , which depends on time-parameter  $t$ . A wavelet's family is therefore generated by scaling and shifting of  $\psi(t)$  as follows:

$$\psi_{a,b}(t) = \frac{1}{\sqrt{a}} \psi\left(\frac{t-b}{a}\right) \quad a, b \in \mathfrak{N}, a > 0 \quad (7)$$

where  $a$  and  $b$  are factors standing for scaling and time-shifting, respectively. To force  $\psi(t)$  to be a wavelet function, it must satisfy at least two conditions. First one requires a wavelet to have finite energy, i.e.:

$$\int_{-\infty}^{\infty} |\psi(t)|^2 dt < \infty. \quad (8)$$

Secondly, if the Fourier transform of  $\psi(t)$  is defined as:

$$\hat{\psi}(\nu) = \int_{-\infty}^{\infty} \psi(t) e^{-i2\pi\nu t} dt \quad (9)$$

then the following condition must hold:

$$C_{\psi} = \int_0^{\infty} \nu^{-1} |\hat{\psi}(\nu)|^2 d\nu < \infty. \quad (10)$$

That implies that the wavelet does not have a zero frequency component, i.e.  $\hat{\psi}(0) = 0$ . It simply means that, for  $\psi(t)$  to be a wavelet, it must have a zero mean:

$$\int_{-\infty}^{\infty} \psi(t) dt = 0. \quad (11)$$

This relation constitutes the subject of *admissibility condition* whereas  $C_{\psi}$  is called the admissibility constant. Its value changes depending on a choice of wavelet function we make. Under the restriction of (11)  $\psi(t)$  displays an oscillatory character what justifies its name: a wavelet. Please note that transformation (7) leaves the shape of  $\psi(t)$  invariant and the normalization by  $a^{-1/2}$  ensures a wavelet to have the same energy at each scale.

A set of wavelets to extract from is large. They differ by a shape, width and properties such as (non)orthogonality and complex or real-valued form. A particular selection of wavelet ought to depend both on the nature of signal and type of variability we expect to detect. There are three most

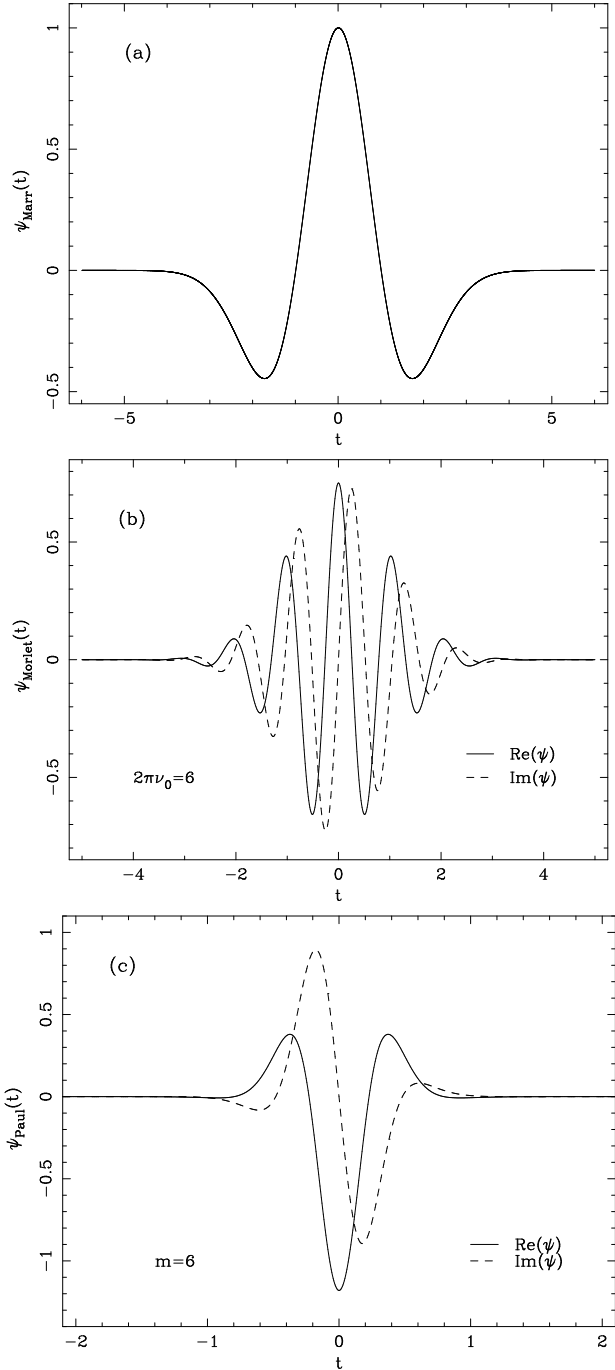


**Figure 2.** Examples of mother wavelets: (a) Marr wavelet; (b) Morlet wavelet; (c) Paul wavelet. The real and imaginary parts of complex wavelets were plotted by solid and dashed lines, respectively.

commonly used wavelets in astronomical time-series analysis: (a) a Marr or Mexican Hat:

$$\psi_{\text{Marr}}(t) = (1 - t^2)e^{-t^2/2} \quad (12)$$

which is a second ( $m = 2$ ) derivative of a Gaussian:

$$\psi(t, m) = (-1)^{m+1} \frac{d^m}{dt^m} e^{-t^2/2}, \quad (13)$$

(b) a Morlet wavelet:

$$\psi_{\text{Morlet}}(t) = \pi^{-1/4} e^{i2\pi\nu_0 t} e^{-t^2/2} \quad (14)$$

which has the complex sinusoidal waveform confined by the Gaussian bell envelope (Grossman & Morlet 1984), and (c) a Paul wavelet:

$$\psi_{\text{Paul}}(t) = \frac{2^m i^m m!}{\sqrt{\pi(2m)!}} (1 - it)^{-(m+1)} \quad (15)$$

where  $m$  denotes an order (Paul 1984; Combes, Grossmann & Tchamitchian 1989). These functions are presented in Fig. 2. Application of complex wavelets instead of real-valued ones is required to capture information on amplitude and phase simultaneously. On the other hand, a real-valued functions are useful for isolation of positive and negative modulations as separate peaks in the time-scale plane, making a clear discrimination of sharp features and signal discontinuities possible to resolve.

In our research we are mainly interested in detection and studies of aperiodic flux structures, therefore mostly the Morlet wavelet will be used throughout the paper. As it oscillates due to a term of  $e^{it}$  and owns a complex form it becomes a desired probing tool in tracing and quantifying quasi-periodic modulations at different scales. Note also that in fact the Morlet function does not meet condition of admissibility. However, it is possible to force it to satisfy (11) by adopting the proper value of  $\nu_0$ . A classical choice applied by Morlet imposes  $\int_{-\infty}^{\infty} \psi_{\text{Morlet}}(t) dt$  to be close to zero for  $2\pi\nu_0 \simeq 5.4$ . Therefore, a small number of oscillations within the Gaussian envelope is allowed. In practice one uses value of 5 or 6. Here we shall adopt  $2\pi\nu_0 = 6$ .

### 3.2.2 Wavelet power spectrum

Making projection of time-series  $x(t)$  onto the family of functions  $\psi_{a,b}(t)$  one can obtain a time-scale representation of the signal defined as a *continuous wavelet transform*<sup>3</sup> (CWT):

$$w_{a,b} = \langle x, \psi_{a,b} \rangle = \int_{-\infty}^{\infty} x(t) \psi_{a,b}^*(t) dt \quad (16)$$

where  $*$  denotes complex conjugate. Therefore, the wavelet coefficients  $w_{a,b}$  are obtained by integration over time the signal multiplied by the wavelet function of finite and short duration. Due to the fact that  $\psi_{a,b}(t)$  function is localized in time-scale plane it allows to fit and capture any local flux modulation. However, because of this property, a certain spread in time and frequency distribution is associated. In general, considering energy density of wavelet function in time and frequency domain,  $|\psi_{a,b}(t)|^2$  and  $|\hat{\psi}_{a,b}(\nu)|^2$  respectively, where the latter denotes the Fourier transform of  $\psi_{a,b}(t)$ , their spread can be quantified by standard deviations around their means, i.e.  $\sigma_t$  and  $\sigma_\nu$ , respectively. For any localization of wavelet, the  $\sigma_t \sigma_\nu \geq (4\pi)^{-1}$  condition must be satisfied. An increase in the wavelet width

<sup>3</sup> Another class of wavelet transforms constitutes *Discrete Wavelet Transform* (DWT) which compact representation is better suitable for application to data compression or purposes of signal de-noising (see e.g. Graps 1995; Romeo, Horellou & Bergh 2004).

corresponds to decrease in spread of spectral component. Therefore, for large scales (low Fourier frequencies) one obtains higher resolution of oscillating flux component in scale whereas for low scales (high Fourier frequencies) accurate time position is better known rather than its frequency. Boxes of area  $4\sigma_t \sigma_\nu$  are known as Heisenberg boxes and relate directly to Heisenberg uncertainty principle mentioned by us in Section 3.1. Please note that while for the wavelet approach the side lengths of Heisenberg boxes depend on scale, for WFT they remain constant.

For discretely defined time-series  $x_k$ ,  $k = 0, \dots, N_{\text{obs}} - 1$ , the continuous wavelet transform (16) can be denoted in its discrete form as:

$$w_k(a) = \sqrt{\frac{\Delta t}{a}} \sum_{k'=0}^{N_{\text{obs}}-1} x_{k'} \psi^* \left[ \frac{(k' - k)\Delta t}{a} \right] \quad (17)$$

where  $\Delta t$  is the sampling time of the lightcurve,  $k$  represents localized time index and a factor of  $\sqrt{\Delta t/a}$  ensures that the following normalization condition:

$$\int_{-\infty}^{\infty} \psi \left[ \frac{(k' - k)}{a} \right] \psi^* \left[ \frac{(k' - k)}{a} \right] dk' = a \quad (18)$$

is satisfied, i.e. the wavelet contains the same energy everywhere in time-scale space of  $w_k(a)$  coefficients. In practice, there is no need to use formula (17) for the calculation of wavelet transform. It can be expressed in terms of the inverse Fourier transform of the product of the Fourier transforms of the signal and wavelet function as given by equation (A10) (see Appendix A for details). For that form, to obtain  $w_k(a_m)$  coefficients, all what is needed to be computed is just  $\hat{x}_j$  (equation 3). Therefore, for lightcurves with equal spacing of  $\Delta t$ , an application of Fast Fourier Transform (FFT) can be implemented at hand.

A *wavelet power spectrum* can be simply defined as normalized square of the modulus of the wavelet transform:

$$W = \xi |w_{a,b}|^2 \equiv \xi |w_k(a_m)|^2. \quad (19)$$

A choice of normalization factor can be done arbitrarily where the most convenient way is to set  $\xi = \sigma^{-2}$ , i.e. equal to the inverse square of lightcurve variance. Here,  $\sigma^2$  represents the expectation value of wavelet transform for a white-noise process at each scale  $a_m$  and time location  $k$  (TC98). The local wavelet power spectrum  $W$  with  $\xi = \sigma^{-2}$  is distributed as  $\chi_2^2$ , i.e. as  $\chi^2$  distribution with two degrees of freedom, therefore it allows to determine the contours at given confidence level for every flux oscillation. A reality of any peak in the wavelet map is tested against certain background spectrum and thus any peak can be accepted or rejected at earlier assumed significance level. At this point, in our analysis, we follow the TC98's selection of background spectrum defined by equation (16) in TC98 and assume 90% confidence level of all drawn contours.

Unfortunately, computation of wavelet power spectrum is not free from errors. They occur at both sides of wavelet map and are related to finite duration of a lightcurve. To omit multiplication of wavelet function with signal at the edges one extends a time-series beyond its original span. A number of methods were proposed to cope with this problem e.g.: zero padding (adding a line of zero values), value padding (adding a line of constant values), decay padding (adding some form of decay to zero), etc. All of them can be introduced for more smooth calculation of  $W$ . In the wavelet

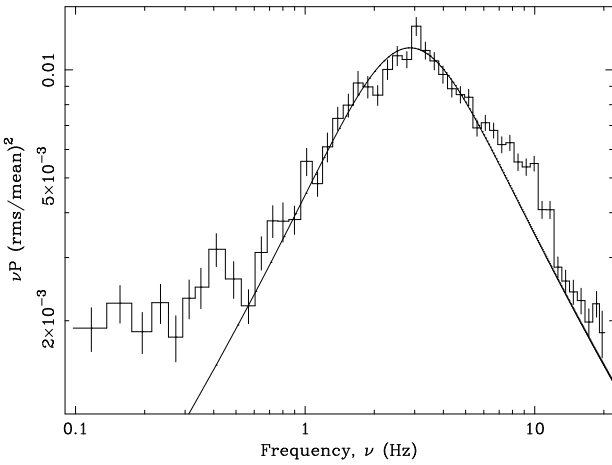


**Figure 3.** Fourier power spectrum of Cyg X-1 on Dec 5, 1999. Solid line represents a broad Lorentzian peak fitted by Pottschmidt et al. (2003).

map, the edge effects result in the so-called *cone of influence*. This cone was defined by TC98 as a region of wavelet map where wavelet power in the vicinity of signal discontinuity decreases by the factor of  $e^{-2}$  and ensures that the edge effects are negligible beyond this region. In our work we apply the simplest solution, i.e. zero padding. As shown recently by De Moortel, Munday & Hood (2004), padding the time-series with additional zeros can be qualitative way in improving the accuracy of the results.

Continuous wavelet transform can be inverted when condition of  $C_\psi < \infty$  is satisfied. Thus, the signal can be reconstructed according to:

$$x(t) = C_\psi^{-1/2} \int_0^\infty \int_{-\infty}^\infty \frac{1}{\sqrt{a}} \psi\left(\frac{t-b}{a}\right) w_{a,b} \frac{db}{a^2} \quad (20)$$

(Grossman & Morlet 1984; for discrete form see TC98). An inverted wavelet transform can work as excellent bandpass filter. By choosing the proper range of scales, say  $(a, a+\Delta a)$ , we are able to extract the shape of signal in this band. An influence of variable components of low- and high-frequency will be hence suppressed.

2-D information about signal in the wavelet map also allows us to compare it to the results of Fourier power spectrum. It can be achieved by performing an integration of wavelet spectrum over time:

$$G(a) = \int |w_{a,b}|^2 db \quad (21)$$

which is known under the name of *global wavelet (power) spectrum* or *scalegram* technique (Scargle et al. 1993). Its discrete form can be denoted as:

$$G(a_m) = \frac{\xi}{N_{\text{obs}}} \sum_{k=k_1}^{k_2} |w_k(a_m)|^2 \quad (22)$$

where  $0 \leq k_1 < k_2 \leq N_{\text{obs}} - 1$  and  $\xi$  denotes normalization factor. Here,  $k_1$  and  $k_2$  ought to be chosen to lie outside the cone of influence for particular scale  $a_m$ . Since normalization can be arbitrary, one can choose it the same as for wavelet power spectrum (e.g.  $\xi = \sigma^{-2}$ ) and therefore determine the proper significance levels (see TC98 for details). If so, when a comparison of (22) with calculated X-ray Fourier power

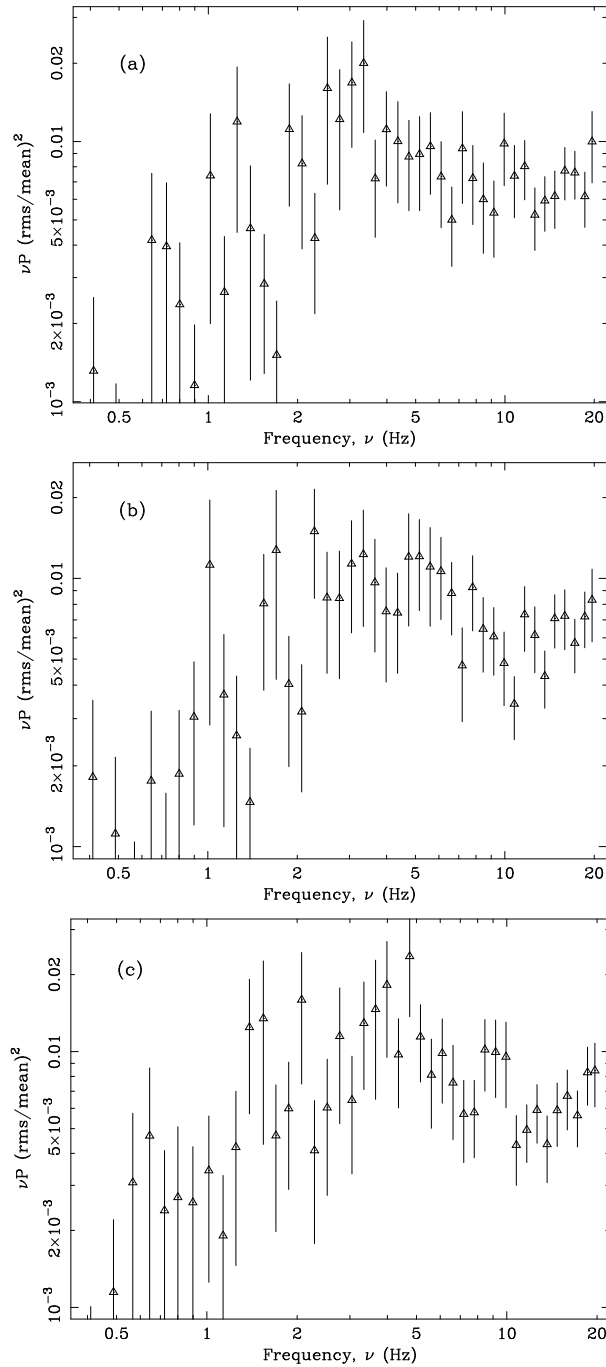


**Figure 4.** Exemplary power spectra calculated for single consecutive data streams of duration 20 s corresponding to the PCA lightcurve intervals: (a) 1090–1110 s, (b) 1110–1130 s, (c) 1130–1150 s. For purposes of comparison with global wavelet power spectra in Fig. 5, the subtraction of noise level was not applied.

spectrum (2) is required, it is possible to adopt normalization factor of the wavelet spectrum  $\xi = 2\Delta t/\bar{x}^2$ . Thus, the global wavelet power spectrum will have the units of  $(\text{rms}/\text{mean})^2/\text{Hz}$ .

We would like also to mark that relation between wavelet scale  $a$  and Fourier frequency  $\nu$  differs and depends on our choice of wavelet function. For Morlet function with assumed  $2\pi\nu_0 = 6$  it holds  $\nu_{\text{Morlet}} \simeq (1.03a)^{-1}$ , for real-

valued Marr wavelet  $\nu_{\text{Marr}} \simeq (3.97a)^{-1}$  whereas for Paul wavelet ( $m = 6$ )  $\nu_{\text{Paul}} \simeq (0.97a)^{-1}$ . Hereafter, y-axes for all of our wavelet maps will be expressed as frequency, given by the above transformations.

## 4 RESULTS

The selected data set covers 1364 s. In Fig. 3 we show the corresponding PSD, together with the dominant Lorentzian component fitted by P03. The shape of the Lorentzian component was described as:

$$L_2(\nu) = \pi^{-1} \frac{2R_2^2 Q_2 \nu_2}{\nu_2^2 + 4Q_2^2(\nu - \nu_2)^2}, \quad (23)$$

and the best fit values of the parameters were: amplitude  $R_2 = 0.188 \pm 0.004$ , center frequency  $\nu_2 = 1.769^{+0.066}_{-0.070}$  Hz, and the quality factor  $Q_2 = 0.395^{+0.032}_{-0.035}$ . This power spectrum component has a maximum at the frequency 2.856 Hz, and the characteristic decay time-scale,  $\tau_2 = Q_2/(\pi\nu_2)$ , is given by  $\tau_2 = 0.07$  s.

The presented PSD shows relatively small errors since the whole time sequence was used. The whole lightcurve was divided into intervals of 25.6 s, the PSD was calculated for each part separately, and finally averaged PSD was plotted, as customary done for such data.

When single PSD spectra are not averaged, they show considerable scatter. For the purpose of further discussion of wavelet maps, we show (see Fig. 4) the examples of the PSD obtained for single fragments of the lightcurve of duration 20 s. Errors are large but the Lorentzian shape is still visible. The selection of 60 s long sequence from whole duration of our PCA time-series was done by us randomly, here corresponding to the interval between 1090–1150 s (Fig. 1).

### 4.1 Wavelet maps

We construct the wavelet maps for the same parts of the lightcurve as used in PSD analysis. The selected band of scales corresponds to the Fourier frequency range between 1 and 10 Hz, where the Lorentzian has the maximum.

We use the Morlet wavelet, with the standard assumption  $2\pi\nu_0 = 6$  (see Section 3.2.1). This means that we probe the signal with a damped wave performing  $\sim 3$  oscillations.

The result is shown in Fig. 5, for three consecutive parts of the lightcurve. Integrated wavelet spectra are shown to the right of each of the sequences.

In all maps many localized strong peaks are seen, standing clearly out of the background. This is even better seen in 3-D plot (see Fig. 6, upper panel). Those peaks dominate the integrated spectrum although they are present only occasionally, mostly between 2–5 Hz. Many lower but still significant peaks are also present, so active phase with significant peaks covers more than half of the observed time. No single frequency seems to be favored and we do not see any particular evolutionary trend. The largest peaks extend in time typically for  $\sim 1$  s which means that they are practically unresolved. Those which extend for a few seconds can be elongated either in the direction of lower or higher frequencies, and the shapes are rather irregular.

We analyzed the distribution and the properties of the

**Table 1.** Properties of the localized peaks in wavelet maps.

Sequence	Cyg X-1	Simulated lightcurve
<i>Number of localized peaks</i>		
Seq. 1	18	11
Seq. 2	16	16
Seq. 3	17	12
<i>Activity level, <math>\kappa</math>, in %</i>		
Seq. 1	63.6	51.2
Seq. 2	59.9	59.5
Seq. 3	62.3	67.9
<i>Median of peak duration, <math>\Delta T_p</math>, in [s]</i>		
Seq. 1	0.54	0.54
Seq. 2	0.54	0.45
Seq. 3	0.27	0.54
<i>Median of peak width, <math>\Delta \log \nu_p</math></i>		
Seq. 1	0.12	0.13
Seq. 2	0.14	0.11
Seq. 3	0.14	0.15
<i>Median of peak frequency, <math>\nu_p</math>, in [Hz]</i>		
Seq. 1	3.7	3.9
Seq. 1	4.3	3.8
Seq. 3	5.2	2.8
<i>Peak width, <math>\Delta \log \nu_h</math>, of the highest peak</i>		
Seq. 1	0.25	0.23
Seq. 2	0.21	0.35
Seq. 3	0.39	0.47
<i>Peak duration, <math>\Delta T_h</math>, of the highest peak in [s]</i>		
Seq. 1	1.1	1.2
Seq. 2	2.8	1.6
Seq. 3	2.7	2.7
<i>Peak frequency, <math>\nu_h</math>, of the highest peak in [Hz]</i>		
Seq. 1	3.4	2.2
Seq. 2	2.1	1.7
Seq. 3	1.4	1.5

significant peaks present in the observational data. The results are given in Table 1. For the analysis, we took only those peaks which are well determined, i.e. detected with 90% confidence level and not extending beyond the studied frequency range. We give there the number of such localized peaks in each of the three sequences. We define the activity level,  $\kappa$ , in each sequence as the fraction of time when at least one peak at any frequency is present. We determine the median value of the logarithm of the frequency,  $\Delta \log \nu_p$ , the median of the peak duration,  $\Delta T_p$ , and the median of the peak frequency,  $\nu_p$ . We also choose the highest of the peaks in each sequence and give for such peak its duration,  $\Delta T_h$ , frequency  $\nu_h$ , and uncertainty of its localization,  $\Delta \log \nu_h$ .

We see that most of the peaks are practically unresolved since their duration and the uncertainty of the frequency is comparable to the Heisenberg limits of the wavelet analysis (see Section 3.1). For the Morlet wavelet with  $2\pi\nu_0 = 6$  the minimum value of  $\Delta \log \nu = 0.11$ , and the minimum value of the time resolution is 0.24 s at 3 Hz (0.71 s at 1 Hz and 0.07 s at 10 Hz). The count rate of the source is high ( $\sim 6000 \text{ cts s}^{-1}$ ) which allows to reach the formal limit of the adopted approach.

Searching the whole lightcurve we have found an interesting sequence which is shown in Fig. 7. There seems to be a chain of peaks, systematically moving towards higher frequencies. Such a development could be consistent with propagation of the perturbations towards the gravity cen-

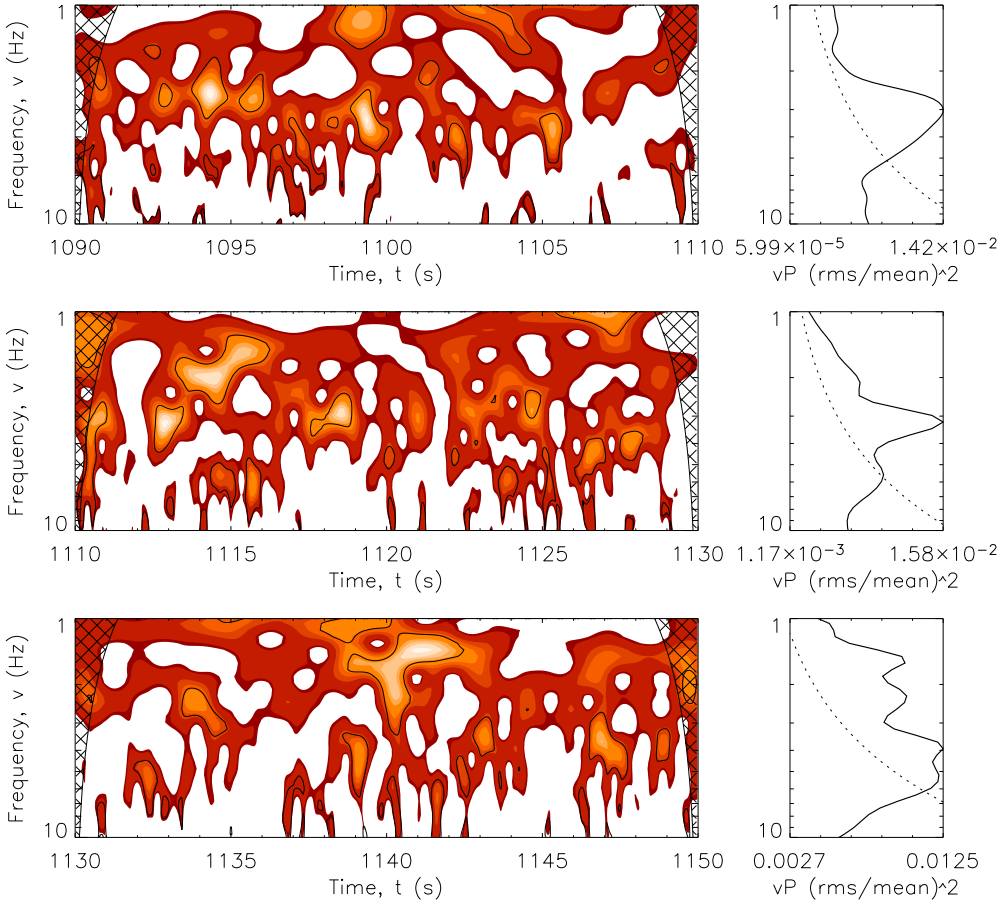


**Figure 5.** (Left panels) Wavelet power spectra of Cyg X-1 during its failed state transition on 1999.12.05 mapping time–frequency evolution of  $\sim 3$  Hz quasi-periodic feature (calculated for randomly selected 60 s time interval from the PCA time-series). Top values of wavelet power are denoted by gradual brightening of the color. Black solid contours denote significance level of 90% for detected peaks. 3-D visualization of the 1090–1110 s wavelet map is shown in Fig. 6. Cone of influence is marked as dashed region. (Right panels) Corresponding global wavelet power spectra, drawn as integrated over time wavelet power spectrum multiplied by frequency (see Fig. 4 for comparison with the Fourier PSD of the same time sequences). Dotted lines represent the 95% significance level calculated according to the procedure given in TC98.

ter, with the expected time-scales decreasing with the radius. More detailed discussion of this sequence we provide in Section 5.7.

## 5 DISCUSSION

The nature of the short time-scale variability in X-ray emission of accreting binaries is still under discussion. The PSD is generally broad-band so the variability is successfully modeled as a shot noise (Terrell 1972; Lehto 1989). Later, more specific models with some physical background were developed (disk turbulence, Nowak & Wagoner 1995; magnetic flares in the disk corona, Poutanen & Fabian 1999, Źycki 2002; propagation of perturbations in the inner hot flow, Böttcher & Liang 1999, Źycki 2003; perturbations in the accretion rate in the cold disk, Mineshige, Ouchi & Nishimori 1994, Lyubarskii 1997). Differentiation between those models is very difficult.

Occasionally, the power spectrum shows a hint of a single oscillation which dominates the variability. Such a sit-

uation happens during a transition state. Careful study of this apparently simple state should reveal the nature of variations more easily. For example, during a failed transition state, the PSD of Cyg X-1 was quite well represented by a single Lorentzian peak (P03).

Such a single Lorentzian peak represents a damped coherent oscillation with a time-independent frequency. This damping is responsible for the width of the peak. However, similarly broad power spectrum can in principle result from oscillations which are not so strongly damped but which change the frequency with time, like in case of a chirp signal (see e.g. Cohen 1995). Such a change in oscillation frequency may be, for example, connected with the accretion process: if the wave or hot plasma moves inward, the local characteristic scales may decrease with radius.

The Fourier analysis cannot differentiate between the damped oscillation and the modulated frequency. Therefore, in order to search for the underlying physical process we need more advanced method of the analysis.

In this paper we applied wavelet analysis to the Cyg X-1 lightcurve. The wavelet maps show that strong, well local-

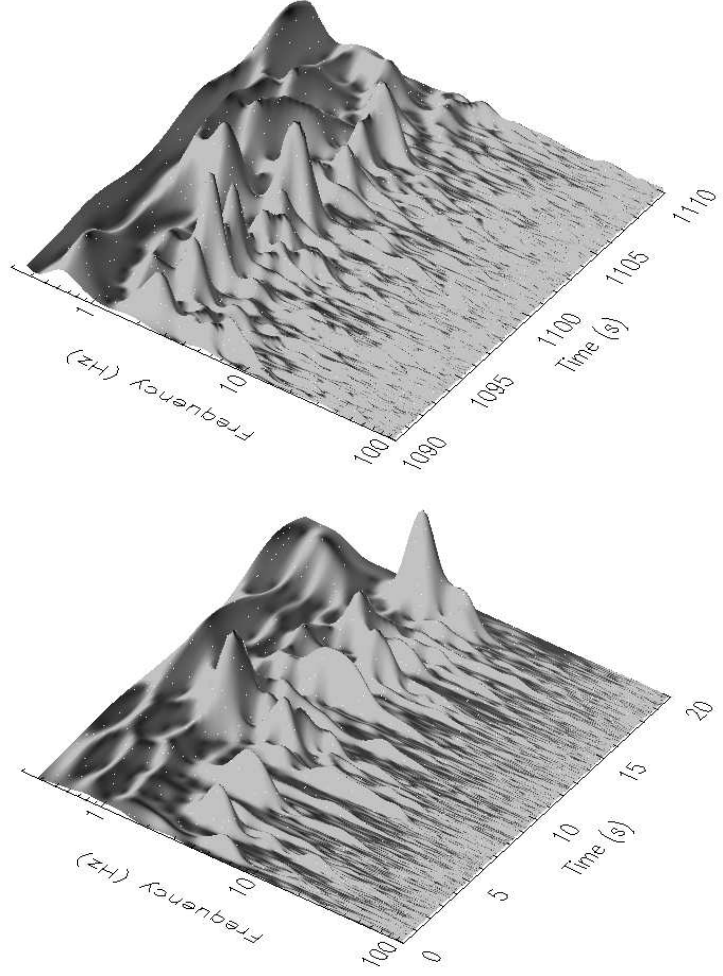


**Figure 6.** 3-D presentation of wavelet power spectrum: (upper) for 20 s long PCA lightcurve; (bottom) for 20 s segment from simulated lightcurve containing randomly occurring flares characterized by Lorentz profile (see Section 5.1). In order of visualization of wavelet power distribution up to 100 Hz, maps were calculated for lightcurves with bin time of  $\Delta t = 2^{-9}$  s.

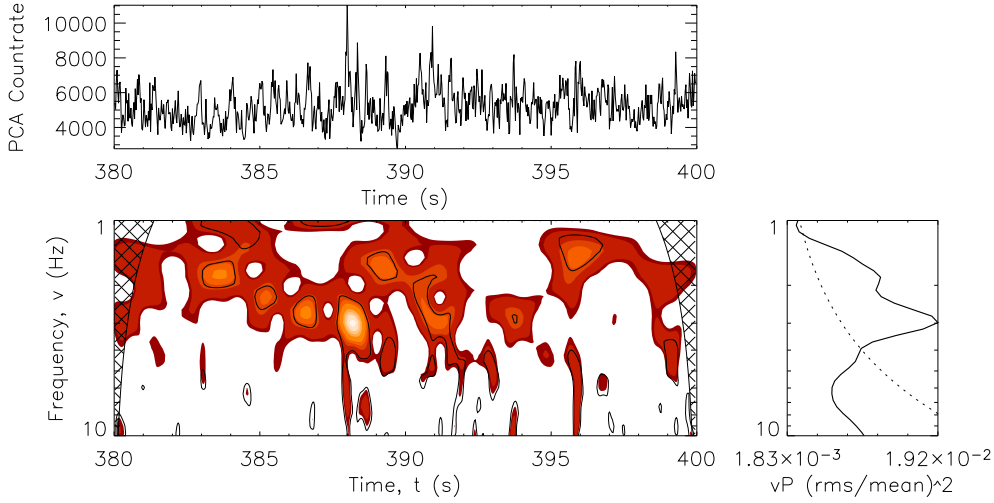


**Figure 7.** (Central panel) Wavelet power spectrum of Cyg X-1 revealing a puzzling chain of peaks ranging between 383–390 s of the analyzed PCA lightcurve (top panel). In the right, corresponding global wavelet power spectrum. See Section 5.7 for discussion.

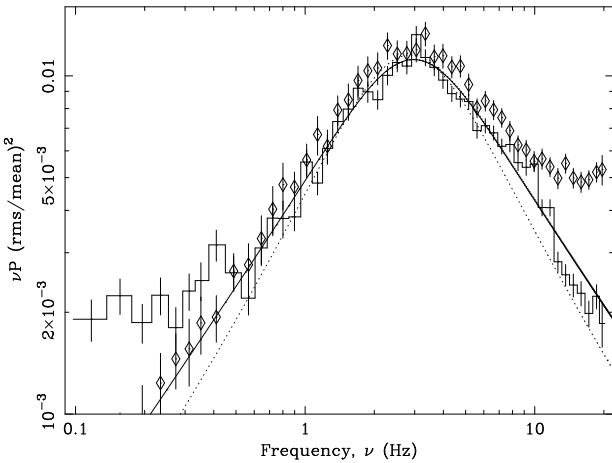


**Figure 8.** Comparison of the fits to the PCA power spectrum performed by Pottschmidt et al. (2003) (dotted line) and provided by application of equation (25) (solid line). Diamond markers denote power spectrum calculated from 1000 s long simulated lightcurve (see Section 5.1).

ized oscillations are present rather occasionally, at frequencies  $\sim 3-5$  Hz and they typically last for  $\sim 0.3-0.5$  s. A few such strong peaks are always present in each of the 20 s sequences and they effectively determine the character of variability, although some peaks above the 90% confidence threshold are typically seen for more than half of the observation time. We did not find any systematic frequency change in oscillations. The analysis gave an upper limit on the rate of the frequency change during a single oscillation  $\delta \ln \nu_0 / \delta \ln t \leq 0.2$ .

This result supports the option of a coherent oscillation with strong damping present in the system. However, in order to analyze more qualitatively the description of the system as a dumped oscillator we performed numerical simulations.

### 5.1 Simulated lightcurves

In order to model the observed lightcurve dominated by the Lorentzian peak we basically follow the approach of Źycki (2003). We create a simulated lightcurve as a superposition of the random shots with the shape:

$$F(t) = A_i e^{-(t-t_i)/\tau} \cos[2\pi\nu_2(t-t_i) + \phi_i] \quad \text{for } t > t_i, \quad (24)$$

and  $F(t) = 0$  for  $t < t_i$ . The values of the frequency  $\nu_2$  and of the characteristic time-scale  $\tau$  were fixed, i.e. the same for all shots. The amplitude of a shot,  $A_i$  was assumed to cover uniformly the range between 0 and  $A_0$ , the shot phase,  $\phi_i$ , was assumed to be distributed uniformly between 0 and  $2\pi$ . The moments of shot appearance,  $t_i$ , were chosen from the Poisson distribution, for an assumed mean frequency of shot generation,  $\lambda$ . It means that the time separation between the consecutive flares,  $\delta t = t_{i+1} - t_i$ , was given by  $\delta t = -\log(\text{rand})/\lambda$  where  $\text{rand}$  is a random number between 0 and 1.

It is easy to show that such a lightcurve is characterized by a power density spectrum:

$$\mathcal{P}(\nu) = \frac{C}{\tau^{-2} + 4\pi^2(\nu - \nu_2)^2} + \frac{C}{\tau^{-2} + 4\pi^2(\nu + \nu_2)^2} \quad (25)$$

The first term has the Lorentzian shape, as requested. The second term is a smooth and slowly varying function so the sum of these two terms has roughly the Lorentzian shape, as requested. We cannot have a better representation of a Lorentzian power spectrum since the power spectrum of a real function in the time domain must have a power spectrum symmetric in frequency. The Lorentzian shape itself is not symmetric so it corresponds to unphysical complex function in the time domain.

This complication means that formally we cannot use the published values of the Lorentzian peak parameters in order to generate the simulated lightcurve with the same power spectrum. Instead, we should refit the original power spectrum with the new function given by equation (25). Since this shape is not strongly different from a Lorentzian (see Fig. 8), it represents the data equally well. The new values of the constants involved are:  $C = 0.945 \pm 0.065$ ,  $\nu_2 = 1.817 \pm 0.184$  Hz,  $\tau = 0.067 \pm 0.003$  s. New value of the frequency and the damping time-scale are only slightly different from the values obtained by P03 from fitting a single Lorentzian peak (1.769 Hz and 0.07 s, correspondingly).

The lightcurve given by equation (24) has statistically zero mean so we must add the value representing the mean count rate,  $\bar{x}$ , in the PCA observation. The coefficients  $A_0$  and  $\lambda$  must be chosen in such way that the resulting lightcurve has the required rms, the same as PCA data. Interestingly, we found that there exists a whole family of parameters  $(A_0, \lambda)$  which reproduce the required normalization of the power spectrum since the constant  $C$  in equation (25) is given by:

$$C \propto \frac{A_0^2 \lambda}{\bar{x}^2} \quad (26)$$

what implies that the following relation:

$$A_0^2 \lambda = \text{const} \quad (27)$$

holds for every couple of  $(A_0, \lambda)$  at assumed mean count rate,  $\bar{x}$ , and fractional rms variability.

We also included the white noise in our simulated lightcurve. For this purpose, in each of the time bins of the simulated time-series we calculate the number of photons, we treat this value as 'average', draw an actual number of counts from the Poisson distribution around this value and finally we divide this value by the bin size in order to return to count per second units. It can be shortly written as:

$$F_N(t) = \text{POISDEV}[F(t)\Delta t]/\Delta t. \quad (28)$$

Above,  $F(t)$  is given by equation (24),  $\text{POISDEV}$  represents a subroutine which generates a random number with Poisson distribution (Press et al. 1992) and thus  $F_N(t)$  denotes simulated lightcurve with Poisson noise level included.

The level of noise does not depend on a specific choice of a pair  $(A_0, \lambda)$  if it satisfies the relation (27). However, created lightcurves differ visually: low  $\lambda$  naturally result in rare steep peaks while high  $\lambda$  give apparently very noisy curve without clear pattern. Visually, lightcurves created with  $\lambda \sim 20-30$  look most similar to the observed lightcurve of Cyg X-1. We will return to this point later.

### 5.2 Wavelet maps for simulated lightcurves

We generated 1000 s long lightcurve,  $F_N(t)$ , with assumed parameters:  $\tau = 0.067$  s,  $\lambda = 20$ ,  $A_0 = 2500$  cts s<sup>-1</sup> and

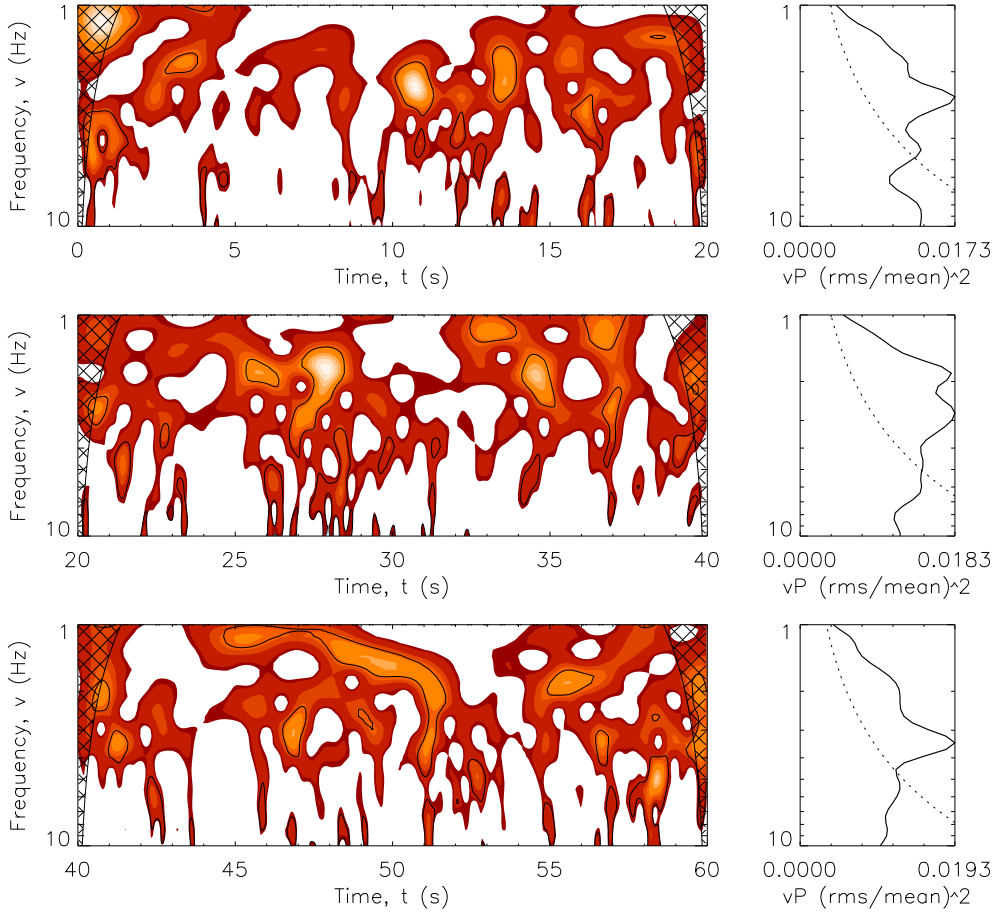


**Figure 9.** (Left panels) Wavelet power spectra of a simulated lightcurve ( $\lambda = 20$ ,  $A_0 = 2500 \text{ cts s}^{-1}$ ) calculated for randomly selected 60-second time interval. Top values of wavelet power are denoted by gradual brightening of the color. Black solid contours denote significance level of 90% for detected peaks. Cone of influence is marked as dashed region. (Right panels) Corresponding global wavelet power spectra, drawn as integrated over time wavelet power spectrum multiplied by frequency. Dotted lines represent the 95% significance level.

$\nu_2 = 1.817 \text{ Hz}$ . The mean count rate of our simulated time-series yielded to be equal  $6081.8 \text{ cts s}^{-1}$  whereas fractional rms 21.9%. In the first step we computed PSD to check whether such composed lightcurve is able to reproduce observed shape of power spectrum from the PCA data. Result of it has been presented in Fig. 8 by diamond markers. As one can see, the shape and the width of PSD of simulated time-series agrees very well with main spectral component of Cyg X-1 PSD.

Next, from  $F_N(t)$  we again chose randomly three sequences, 20 s each, for the wavelet analysis. The wavelet maps for the simulated lightcurve are shown in Fig. 9. 3-D picture of exemplary series is shown in the bottom panel of Fig. 6.

The maps are very similar to those obtained from the data analysis. This can be even better seen from quantitative parameters given in Table 1. Peaks in the maps for simulated lightcurves also are distributed in a broad frequency range.

At first sight this result may seem puzzling. Since the basic frequency in the simulated lightcurve is fixed, we might expect better localization of the peaks in frequency. However, the random choice of the phase, together with ex-

tremely strong damping, creates an apparent diversity of the shapes among the consecutive shots, leading to relatively broad peaks, at broad frequency range, as in the data.

Closer inspection suggests also certain systematic differences. Simulated lightcurves create slightly fewer peaks in the maps, and the median frequency in the data is somewhat higher. This is most probably related to an excess of the power at high frequencies above a single Lorentzian peak seen in the data ( $\sim 8\text{--}12 \text{ Hz}$ , see Fig. 3). Otherwise, all properties of the observed lightcurve are well represented.

We also analyzed simulated lightcurves assuming lower and higher values of  $\lambda$  (with appropriate  $A_0$  given by relation (27)). Maps for significantly larger or significantly smaller values of  $\lambda$  were different from the maps for Cyg X-1. Most noticeably, the activity level shortened to 45% for  $\lambda = 5$  and 55% for  $\lambda = 55$ ; it was 59.5% for  $\lambda = 20$  and 61.9% in the data maps. Therefore, wavelet maps give constraints for  $\lambda$ , although they are not very sensitive to its choice.

We tested the map sensitivity to the adopted bin size in the data and in the simulations. Adopting bin size of  $\Delta t = 2^{-9} \text{ s}$  (i.e. the minimal bin size available in analyzed PCA data set) the noise in the lightcurves (and in the power

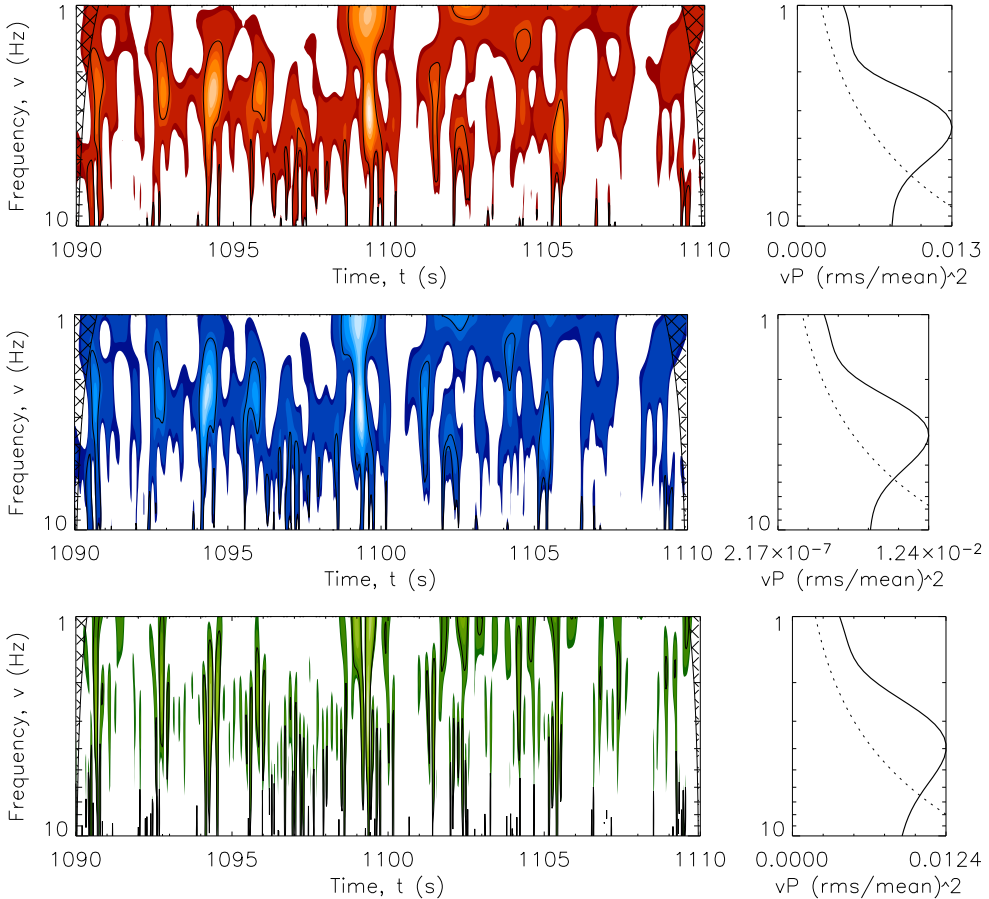


**Figure 10.** Wavelet power spectra of Cyg X-1 corresponding to the PCA data sequence between 1090–1110 s, calculated applying (top panel) Morlet wavelet with  $2\pi\nu_0 = 3$ , (middle panel) Paul wavelet with  $m = 6$  and (bottom panel) Marr wavelet. In the right, corresponding global wavelet power spectra.

spectrum) increased but the maps were barely changed, as already noticed by Liszka, Pacholczyk & Stoeger (2000b).

### 5.3 Morlet wavelet with non-standard parameters and other wavelet shapes

Following the most recent analysis of De Moortel, Mundat & Hood (2004) we tried to increase the time resolution at the expense of frequency resolution by adopting smaller values of  $2\pi\nu_0$ . We constructed the Morlet wavelet map both for the data (see Fig. 10, top panel) and for the simulated lightcurve (map not shown) using  $2\pi\nu_0 = 3$ . However, in this case we loose the resolution in frequency. Features become more elongated. Again, no pattern in frequency evolution can be seen. The extension of the peaks in the time domain decreased. A systematic difference between the observed and the simulated lightcurve with respect to the number of localized peaks and the extension of active periods remains. Conversely, an attempt in adopting the Morlet parameter  $2\pi\nu_0 > 6$  returned in more precise frequency resolution of existing features at the expense of their time localization (map not shown). Also in this case, the statistics for the

map did not change for the advantage of adopting Morlet function with  $2\pi\nu_0 > 6$ <sup>4</sup>.

We also tried to apply two other wavelet shapes: a Marr and a Paul wavelet. Marr gave a very poor resolution in frequency both for the data (Fig. 10, bottom panel) and for the simulated lightcurve (map not shown), even worse than Morlet wavelet with  $2\pi\nu_0 = 3$ . Most of the peaks were so elongated that they extended beyond the studied frequency range, making this wavelet rather useless for the studied lightcurves. However, it indicated fast disappearance of the peaks, in time-scales shorter than 0.3 s. Also the systematic difference between the observed and the simulated lightcurve was again seen: activity periods in Cyg X-1 covered larger fraction of time than in the simulated time-series.

The Paul wavelet (Fig. 10, middle panel) had effective properties similar to the Morlet wavelet with  $2\pi\nu_0 = 3$ . Therefore, the use of the canonical Morlet shape with  $2\pi\nu_0 = 6$  seems to be indeed the most profitable in the context of the X-ray lightcurves.

<sup>4</sup> Please note that Morlet wavelet with  $2\pi\nu_0 < 5$  and  $> 6$  does not meet admissibility condition (Section 3.2.1) and its usage can be justified only for non-quantitative analysis.

## 5.4 Applicability of a single Lorentzian model to failed transition state

Our wavelet analysis generally supports the interpretation of Cyg X-1 variability during the failed state transition as damped oscillations with fixed underlying frequency. Additional support comes from the recent paper by Feng, Zhang & Li (2004). They apply a different technique to analyze the lightcurve of Cyg X-1 (*w* spectral analysis) which is sensitive to the shortest time-scales present in the system. The resulting time-scales for hard and intermediate state are of the same order as the damping time-scale of the Lorentzian, consistent with the extension of the detected features on our wavelet maps.

Simulated lightcurves gave maps quantitatively similar to the maps obtained from the Cyg X-1 lightcurve. The observed PSD contains an excess of power at higher frequencies (modeled by P03 as an additional Lorentzian peak). Simulated lightcurves did not contain this additional high frequency input but still reproduced the maps properly so the dominant Lorentzian is responsible for the character of the variability both in the frequency domain and in the time-frequency domain.

## 5.5 Dominating PSD components in hard, soft and failed soft state

Our results give a strong support to the interpretation of the PSD through Lorentzian peak during the failed state transition. It means that in general case we most probably deal with three main *physical* components of the PSD with the following properties (Nowak 2000; P03):

- Power law component  $\nu^{-1}$ : this component dominates the PSD at  $\nu < 10^{-5}$  Hz (Reig, Papadakis & Kylafis 2002), it extends up to 15–20 Hz when the source is in soft state, it extends into the region  $\nu \sim 10^{-3}$ –10 Hz but with suppressed amplitude during the transition state and it practically disappears in the hard state;
- Lorentzian peak  $L_1$ : present in the hard state but its amplitude strongly decreases during the transition state, accompanied with the rise of the power law in high frequency range;
- Lorentzian peak  $L_2$ : suppressed only when the the soft state is reached; ratio of the two Lorentzian frequencies is constant ( $\sim 7$ ) although the frequency can change in long time-scale up to a factor of 4.

Results for the coherence function and Fourier time delays support the view that both Lorentzians are generally highly coherent, also between themselves (Nowak et al. 1999) but when one of the peaks disappears in the failed state transition, the mean time delay between 2–4 keV and 8–13 keV increases to 8 ms (a typical value if measured at  $\sim 3$  Hz), and the coherence in 3–10 Hz band drops to 0.6 (P03). Similar properties were observed by Cui et al. (1997b) (e.g. 30.05.1996) when the source was on its way to the completed transition to soft state.

These components seem to be critical for our understanding of the nature of the observed variability although exact fits to the data generally require more components.

## 5.6 Physical interpretation of the X-ray variability

### 5.6.1 Power Law component $\nu^{-1}$ : propagating disk oscillations filtered at the transition radius

There are several independent arguments in favor of the hypothesis that the  $\nu^{-1}$  power law component of the PSD is related to the presence of the cold disk. This component is exclusively responsible for the observed variability when Cyg X-1 is in the soft state, i.e. radiation spectrum is dominated by the disk emission and we see the relativistically broadened iron K $\alpha$  line which gives constraints for the cold disk inner radius (e.g. Di Salvo et al. 2001). The time-scales involved cover uniformly a large range, including time-scales as long as years which are naturally expected in the outer disk. However, there were two puzzles which were not initially understood. First, what we see is *not the variable disk emission*, since the direct disk emission is roughly unchanged but *variable Compton component* (Churazov, Gilfanov & Revnivtsev 2001; Maccarone & Coppi 2002). Second, the energy contained in the longest time-scale variability is considerable while the gravitational energy at the outer edge of the disk is small.

The model which successfully explains the situation is the scenario of propagating perturbations. The idea was nicely outlined by Lyubarskii (1997), although some basic ideas were already contained in the automaton model of Mineshige et al. (1994). More sophisticated approach was developed by King et al. (2004). In this model local perturbations form in the disk as a result of the action of the magnetorotational instability (MRI; Balbus & Hawley 1991). Characteristic frequencies of these perturbations at a give radius  $r$  are somewhat lower than the local Keplerian frequency and can be expressed as:

$$\nu_{\text{mag}} = 20 \left( \frac{5.5}{k_{\text{mag}}} \right) \left( \frac{3R_{\text{Schw}}}{r} \right)^{3/2} \left( \frac{20M_{\odot}}{M} \right) \text{ [Hz].} \quad (29)$$

Most of the authors argued that the inner radius of the disk in the soft state is of order of  $3 R_{\text{Schw}}$  (e.g. Frontera et al. 2001 give  $6_{-0}^{+4} R_g$ , where  $R_g = 0.5R_{\text{Schw}}$ ) and we adopted this value as a convenient unit. The characteristic frequency at this radius reproduces the observed PSD frequency break at 20 Hz in the soft state when  $k_{\text{mag}} = 5.5$ . The factor of  $2\pi$  was included, i.e.  $\nu = \Omega/(2\pi)$ . Those perturbations propagate inward, to the region where dissipation and the production of the hard X-ray emission proceeds. Therefore, the accretion rate at the inner dissipation region has a memory of all time-scales present in the disk at all radii.

When the source proceeds from a soft state to a hard state, the power law component is not seen at time-scales shorter than  $10^{-5}$ – $10^{-3}$  Hz. We cannot relate this change to a change of the disk inner radius since this would require a change of the radius by a factor of  $10^3$ – $10^4$ . Analysis of the data suggest much lower values about e.g.  $\sim 5$ – $35 R_{\text{Schw}}$  (di Salvo et al. 2001),  $10_{-4}^{+5} R_g$  (Frontera et al. 2001) or  $\sim 100 R_g$  (Gilfanov, Churazov & Revnivtsev 2000).

However, a natural explanation of this change is found if we adopt the *strong ADAF principle* after Narayan & Yi (1995). This is a statement which tells that *whenever an ADAF can form, it does form*. The consequence of this assumption is that for a given value of the transition radius,  $r_{\text{tr}}$ , only one value of the accretion rate is possible. This fact

automatically leads to filtering all time-scales in the momentary accretion rate shorter than a local viscous time-scale. If the perturbed accretion rate is somewhat larger than allowed by a current position of the transition radius, the matter accumulates near  $r_{tr}$  while the accretion rate in the inner flow is unperturbed. Mass accumulation, if persisting for long enough, leads to a buildup of a cold disk in part of the region previously occupied by the inner hot flow. The position of the transition radius moves in, and after this change an inner hot flow can transmit mass at higher rate, appropriately to the new position of  $r_{tr}$ . Alternatively, if the perturbed accretion rate in the disk is somewhat lower than current  $r_{tr}$ , the inner hot flow still persists with the same accretion rate at the expense of the cold disk. Finally, the cold material is used up, the transition radius moves out to the new position, and the accretion rate in the inner flow decreases in agreement with new  $r_{tr}$ . Since both the removal and the buildup of the cold disk happens in a local viscous timescale all variations in the accretion rate slower than that are transmitted while faster variations are dumped. The fastest timescale for a transition from a hard to a soft state is also given by a viscous time-scale,

$$\tau_{visc} = 1.5 \times 10^3 \left( \frac{0.01}{\alpha} \right) \left( \frac{0.08r}{h} \right)^2 \left( \frac{r}{50R_{Schw}} \right)^{3/2} \times \left( \frac{M}{20M_{\odot}} \right) \text{ [s]} \quad (30)$$

and it is observationally constrained to be of order of a day, or a fraction of a day, consistent with the time-scale  $10^{-3}$ – $10^{-5}$  Hz. Here we assumed the expected ratio of the disk thickness to the radius,  $h/r$  of order of 0.08 and  $\alpha = 0.01$  after King et al. (2004), for the scaling purposes.

This picture gives a strong observational support to the *strong ADAF principle*. An independent argument for this kind of behavior was also found by Czerny, Różańska & Kuraszkiewicz (2004) from the study of the constraints for an inner radius from Broad Line Region in Active Galactic Nuclei.

During the transition state the accretion rate is most probably much more strongly enhanced than during hard state perturbations. Observations show a sudden decrease in the inner radius. For example, on 1996.05.30, when the state was yet similar to the failed state transition, the inner radius was estimated to be  $9_{-4}^{+13} R_{Schw}$  (Gierliński et al. 1999). However, we can suspect that the material piles up rapidly. Instead of smooth motion of the transition radius clumps of cold material possibly enter the inner hot flow region and accrete. Such a direct accretion of a cold phase may (i) explain why during the transition, including failed transition state, the short time-scale perturbations in the accretion flow start to propagate inward, (ii) cold moving blobs provide additional source of soft photons for Comptonization which disrupt the high coherence seen during the hard state.

It still remains to explain what kind of instability leads to the disk destruction when ADAF solution is possible. An interesting scenario is discussed by Spruit & Deufel (2002), but it requires the initial existence of the hot ions. It may give a hint why we observe a strong hysteresis effect in some sources but not in Cyg X-1. This hysteresis (see e.g. Miyamoto et al. 1995; Meyer-Hofmesiter, Liu & Meyer 2004;

Zdziarski et al. 2004) leads to a transition from soft to hard state at much lower accretion rate than the transition from hard to soft state. In the soft state of Cyg X-1 significant fraction of emission is of non-thermal origin. Hot ions are always there, and the mechanism of Spruit & Derfel (2002) may operate while we need another mechanism for sources which do not show any hot plasma in the soft state.

### 5.6.2 Lorentzian peaks $L_1$ and $L_2$ : MRI and dynamical pulsations of the inner ion torus

The two Lorentzian peaks dominating the hard state are expected to be related to the inner ion torus. The constant ratio between their frequencies strongly suggest that we see two kinds of variability coming from the same medium.

Since the inner hot flow must transport the material the same MRI instability is expected to be operating. Since the inner flow is expected to be geometrically thick, instability has more global character there, and the dominant frequency is likely to be determined by the transition radius. This frequency still should be roughly reproduced by equation (29):

$$\nu_1 = 20 \left( \frac{5.5}{k_{mag}} \right) \left( \frac{3R_{Schw}}{r_{tr}} \right)^{3/2} \left( \frac{20M_{\odot}}{M} \right) \text{ [Hz]} \quad (31)$$

When the second Lorentzian peak is at 1.7 Hz, the first peak is at 0.25 Hz (P03), and such a frequency is reproduced for a reasonable value  $r_{tr} = 55R_{Schw}$ . In general, the position of the Lorentzian varies. Revnivtsev, Gilfanov & Churazov (2001) showed that the corresponding peak in the power spectrum of GX 339-4, described as quasi-periodic oscillation (QPO), strongly correlates with other spectral properties of this source, supporting its connection with the change of the transition radius.

Higher frequency variations are likely to represent the dynamical pulsation of the inner hot flow, or traveling sound waves. Global oscillations of this medium, modeled as a torus, were studied in a number of papers (e.g. Abramowicz, Calvani & Nobili 1983; Giannios & Spruit 2004; Montero, Rezzolla & Yoshida 2004). The typical frequencies of  $p$ -modes depend on the details of the model (e.g. assumed radial distribution of the angular momentum) but they are roughly of the order of the Keplerian frequency at the outer edge of the torus (Rezzolla, Yoshida & Zanotti 2003). The excitation of the modes is due to radiative interaction of the disk and the torus, while synchrotron emission provides the dumping mechanism (Giannios & Spruit 2004).

The expected frequency of this mode is roughly:

$$\nu_2 = 1.62 \left( \frac{50R_{Schw}}{r_{tr}} \right)^{3/2} \left( \frac{20M_{\odot}}{M} \right) \text{ [Hz]} \quad (32)$$

so the value of the transition radius  $\sim 50R_{Schw}$  gives the value of the frequency roughly corresponding to the observed frequency of the Lorentzian, 1.7 Hz.

During the failed transition state the first Lorentzian peak is strongly dumped, and a power law components is partially rebuilt, as discussed in Section 5.6.1. If the first Lorentzian peak is connected with MRI instability, the exchange of power between a power law component and the first Lorentzian is natural. Decreased MRI instability in the inner flow suppress the accretion of the hot material and the accretion proceeds predominantly through cold blobs. It

is an interesting question whether the presence of the cold blobs prevent MRI instability or the absence of hot material accretion forces the cold phase to take over but the eventual compensation of the two mechanisms is quite intuitive. Apparently, dynamical pulsations persist as long as the hot inner torus is still there. If a transition to a soft state is completed, this phase finally disappears.

The suggested picture may be too simple since actually a number of instabilities may operate in the accretion flow (e.g. Menou, Balbus & Spruit 2004 and the references therein) but we consider our interpretation as a plausible and attractive scenario. Clearly, quantitative models would be needed to work out the detailed predictions.

Observationally, an insight may come from the presence of rapid, very energetic events reported by Gierliński & Zdziarski (2003) both during soft and hard state. It is interesting that a soft state flare no. 13, studied in detail by these authors, was found to be well described by damping time-scale (after the peak) of  $\tau = (21 \pm 5)^{0.7 \pm 0.1}$  ms, i.e.  $\tau \simeq 0.07$  s. This damping time-scale is the same as the damping time-scale of the  $L_2$  Lorentzian, may indicate that damping is related to magnetic field reconnections. Same event observed in the hard state yielded much longer damping time-scale,  $\sim 0.32$  s which in turn roughly coincides with the damping time-scale of the first Lorentzian,  $L_1$ . Although the exact origin of the flares is not known, one takes into account sudden conversion of energy accumulated in the disk into magnetic heating of a hot plasma or fast release of energy due to magnetic field reconnection in flares hung above the disk (Gierliński & Zdziarski 2003 and references therein). The difference between the hard state and the soft or failed transition state may be due to the absence of the cold material in the former case. Therefore, in the hard state the large scale magnetic loops exist within the torus, while in the soft state or failed transition state magnetic field lines are partially frozen into the cold disk or cold blobs.

## 5.7 Wavelet analysis as a tool for tracing accreting matter onto black-holes?

It is tempting to associate observed puzzling chain of peak in Fig. 7 (mentioned already by us in Section 4.1) with a systematic trend.

Looking closer in Fig. 7 one can realize that the figure shows up in fact, not one but two ranges of peaks roughly of the same slope. First, most prominent, extending between 383–391 s, whereas the second one between 389–397 s (1.5 Hz  $\rightarrow$  6 Hz). Careful inspection of all 20 s long sequences of analyzed PCA data uncovers more similar *trends* of the same slope. Unfortunately, their number is low (about 14 per whole lightcurve; each of duration  $\leq 7$  s). Interestingly, we found that a preliminary analysis of MCG-6-30-15 lightcurve from 0.2–10 keV *XMM-Newton* observations reveals also analogous trends in wavelet maps. Here, their activity level seems to be much higher.

Comparison of wavelet map in Fig. 7 with corresponding PCA lightcurve shows that all wavelet features are associated with some peaks occurring in the same moments in the time-series, as expected. Moreover, a wide diversity of peak shapes can be read off, similar as in simulated lightcurve (Section 5.1). However, we did not find traces of

evolution from lower to higher frequencies, similar to those in Fig. 7, in the simulated data.

The time–frequency evolution of some features is not totally unexpected. Both the hot ion torus material and cold clumps flow into the black hole, in the direction of decreasing Keplerian time-scales. We can witness trail of single events like a sequence of magnetic field reconnections in inflowing material.

If these enigmatic chains of oscillations are related somehow to physical processes of X-ray emission, then, in our opinion, a wavelet analysis may become a new powerful tool in searching and tracing the *semi-direct* evidences of accreting material onto black-holes in black-hole binaries as well as in AGN. However, we would like to mark that in order to describe observed *trends* in a quantitative way, one needs to develop more sophisticated methods of their statistical description.

## 6 CONCLUSIONS

For the first time, we applied the wavelet multi-resolution approach in order to perform complex studies of aperiodic X-ray variability of Cyg X-1. Considered data set corresponded to its failed state transition on 1999.12.05. On that day, the Fourier power spectrum revealed a broad-band peak between  $\sim 1$ –10 Hz, well described by single Lorentz function of unclear origin. On contrary to Fourier method, wavelet analysis provided excellent inspection of frequency content of the signal as well allowed for simultaneous tracing time evolution of extracted features.

Our results can be summarized as follows:

- Cyg X-1 lightcurve analyzed in time–frequency plane contained randomly appearing flare-like structures of duration  $\sim 0.5$  s and of the average median of peak frequency width  $\Delta \log \nu_p \simeq 0.14$ ;
- observed Lorentzian shape forms through summation of these time-localized structures;
- most of the Cyg X-1 lightcurve properties are well reproduced by the simulated lightcurve composed of a series of randomly occurring flares. In our model, each flare was described as a damped oscillator with variable amplitude and phase but fixed excitation frequency and time-scale of decay;
- Cyg X-1 wavelet maps may show trail of inflow while the maps representing the simulated lightcurve do not seem to show similar tendency. However, no statistical significance was assigned to this hypothesis.

## ACKNOWLEDGMENTS

The work dedicated in memory of Prof. Edward Wilk. We thank Chris Torrence for many helpful and friendly discussions on wavelets and Piotr Źycki for valuable remarks. We also thank Gabriele Ponti for kind providing of the *XMM-Newton* data. The wavelet software was provided by Christopher Torrence and Gilbert P. Compo and it is available at <http://paos.colorado.edu/research/wavelets>. We also acknowledge the use of data obtained through the HEASARC online service provided by NASA/GSFC.

## REFERENCES

Abramowicz M., Calvani M., Nobili L., 1983, *Nat.*, 302, 597

Angelini L., White N., Stella L., 1992, *IAU Circ.* No. 5580

Aschwanden M.J., Kliem B., Schwarz U., Kurths J., Dennis B.R., Schwartz R.A., 1998, *ApJ*, 505, L941

Balbus S., Hawley J.F., 1991, *ApJ*, 376, 214

Barreiro R.B., Hobson M.P., 2001, *MNRAS*, 327, 813

Belloni T., Hasinger G., 1990, *A&A*, 227, L33

Bolton C. T., 1972, *Nature*, 235, 271

Böttcher M., Liang E.P., 1999, *ApJ*, 511, L37

Bowyer S., Byram E.T., Chubb T.A., Friedman H., 1965, *Science* 147, 394

Bradt H.V., Rothschild R.E., Swank J.H., 1993, *A&AS*, 97, 355

Churazov E., Gilfanov M., Revnivtsev M., 2001, *MNRAS*, 321, 759

Cohen, L. 1995, Time-frequency analysis, Englewood Cliffs, NJ: Prentice-Hall

Combes J.M., Grossmann A., Tchamitchian P., 1989, eds. Wavelets, Time-Frequency Methods and Phase Space, 1st Int. Wavelet Conf., Marseille, Dec. 1987, Inverse Probl. Theoret. Imaging, Springer

Cui W., Heindl W.A., Rothschild R.E., Zhang S.N., Jahoda K., Focke W., 1997a, *ApJ*, 474, L57

Cui W., Zhang S.N., Focke W., Swank J.H., 1997b, *ApJ*, 484, 383

Czerny B., Różańska A., Kuraszkiewicz J., 2004, *A&A* (in press); astro-ph/0403507

Daubechies I., 1992, Ten Lectures on Wavelets, Philadelphia PA: Society for Industrial and Applied Mathematics, 357pp

De Moortel I., Munday S.A., Hood A.W., 2004, *SoPh*, 222, 203

Di Salvo T., Done C., Życki P.T., Burderi L., Robba N.R., 2001, *ApJ*, 547, 1024

Escalera E., MacGillivray H.T., 1995, *A&A*, 298, 1

Farge M., 1992, *AnRFM*, 24, 395

Feng H., Zhang S.-N., Li T.-P., 2004, *ApJ*, 612, L45

Flandrin P., 1999, Time-Frequency/Time-Scale Analysis, Academic Press

Freeman P.E., Kashyap V., Rosner R., Lamb D.Q., 2002, *ApJS*, 138, 185

Frick P., Galyagin D., Hoyt D.V., Nesme-Ribes E., Schatten K.H., Sokoloff D., Zakharov V., 1997, *A&A*, 328, 670

Fritz T., Bruch A., 1998, *A&A*, 332, 586

Frontera F., Palazzi E., Zdziarski A.A., Haardt F., Perola G.C., Chiappetti L., Cusumano G., Dal Fiume D., Del Sordo S., Orlandini M., 2001, *ApJ*, 546, 1027

Garcia-Lorenzo B., Fuensalida J.J., Munoz-Tunon C., Mendizabal E., 2004, astro-ph/0410559

Giannios D., Spruit H.C., 2004, *A&A*, 427, 251

Gierliński M., Zdziarski A.A., Poutanen J., Coppi P.S., Ebisawa K., Johnson W.N., 1999, *MNRAS*, 309, 496

Gierliński M., Zdziarski A.A., 2003, *MNRAS*, 343, L84

Gies D.R., Bolton C.T., 1986, *ApJ*, 304, 371

Gilfanov M., Churazov E., Revnivtsev M., 2000, *MNRAS*, 316, 923

Gleissner T., Wilms J., Pottschmidt K., Nowak M.A., Staubert R., 2004, *A&A*, 414, 1091

Grafs A., 1995, An Introduction to Wavelets, IEEE Computational Sciences and Engineering, Volume 2, Number 2, pp 50-61

Gray D.F., The observation and analysis of stellar photospheres, 1976, John Wiley & Sons, A Wiley-Interscience Publication

Grossman A., Morlet J., 1984. Decomposition of Hardy functions into square integrable wavelets of constant shape. Society for Industrial and Applied Mathematics Journal on Mathematical Analysis, 15:732-736

Herrero A., Kudritzki R.P., Gabler R., Vilchez J.M., Gabler A., 1995, *A&A*, 297, 556

Irastorza I.G., Morales A., Cebria S., Garc E., Morales J., Ortiz de Solorzan A., Osetrov S.B., Puimedro J., Sarsa M.L., Villar J.A., 2003, *APh*, 20, 247

King A.R., Pringle J.E., West R.G., Livio M., 2004, *MNRAS*, 348, 111

van der Klis M., 1989, in Timing Neutron Stars, eds. H. Ogelman and E. P. J. van den Heuvel (Dordrecht: Kluwer), 27

van der Klis M., 1997, Quantifying Rapid Variability in Accreting Compact Objects, in Statistical Challenges in Modern Astronomy II, Proceedings of the conference held 2-5 June, 1996 at Pennsylvania State University. Edited by G.J. Babu and E.D. Feigelson. Berlin: Springer-Verlag, 1997., p.321

Lehto H.J., 1989, in ESA, The 23rd ESLAB Symposium on Two Topics in X Ray Astronomy. Volume 1: X-Ray Binaries, p, 499-503

Liszka L., Pacholczyk A.G., Stoeger W.R., 2000a, *ApJ*, 540, 122

Liszka L., Pacholczyk A.G., Stoeger W.R., 2000b, *A&A*, 354, 847

Lomb N.R., 1976, *Ap&SS*, 39, 447

Lyubarskii Yu.E., 1997, *MNRAS*, 292, 679

Maccarone T., Coppi P.S., 2002, *MNRAS*, 335, 465

Menou K., Balbus S.A., Spruit H.C., 2004, *ApJ*, 607, 564

Meyer-Hofmeister E., Liu B.F., Meyer F., 2004, accepted for *A&A*, (astro-ph/0411145)

Mineshige S., Ouchi B., Nishimori H., 1994, *PASJ*, 46, 97

Miyamoto S., Kitamoto S., Iga S., Negoro H., Terada K., 1992, *ApJ*, 391, L21

Montero P.J., Rezzolla L., Yoshida S., 2004, *MNRAS*, 354, 1040

Miyamoto S., Kitamoto S., Hayashida K., Egoshi W., 1995, *ApJ*, 442, L13

Narayan R., Yi I., 1995, *ApJ*, 452, 710

Nowak M.A., Wagoner R.V., 1995, *MNRAS*, 274, 37

Nowak M.A., Vaughan B.A., Wilms J., Dove J.B., Begelman M.C., 1999, *ApJ*, 510, 874

Nowak M.A., 2000, *MNRAS*, 318, 361

Paul T., 1984, *J. Math. Phys.*, 25, 11

Pottschmidt K., Wilms J., Nowak M.A., Pooley G.G., Gleissner T., Heindl W.A., Smith D.M., Remillard R., Staubert R., 2003, *A&A*, 407, 1039

Poutanen J., Fabian A.C., 1999, *MNRAS*, 306, L31

Press W.H., Teukolsky S.A., Vetterling W.T., Flannery B.P., 1992, Numerical recipes in FORTRAN. The art of scientific computing, Cambridge: University Press, 2nd ed.

Psaltis D., 2004, in "Compact Stellar X-ray Sources", eds. W.H.G. Lewin and M. van der Klis, astro-ph/0410536

Reig P., Papadakis I., Kylafis N.D., 2002, *A&A*, 383, 202

Revnivtsev M., Gilfanov M., Churazov E., 2000, *A&A*, 363, 1013

Revnivtsev M., Gilfanov M., Churazov E., 2001, *A&A*, 380, 520

Rezzolla L., Yoshida S., Zanotti O., 2003, *MNRAS*, 344, 978

Romeo A.B., Horellou C., Bergh J., 2004, *MNRAS*, 354, 1208

Scargle J.D., 1982, *ApJ*, 263, 835

Scargle J.D., Steiman-Cameron T., Young K., Donoho D.L., Crutcher J.P., Imamura J., 1993, *ApJ*, 411, L91

Spruit H.C., Deufel B., 2002, *A&A*, 387, 918

Steiman-Cameron T.Y., Scargle J.D., Imamura J.N., Middleditch J., 1997, *ApJ*, 487, 396

Sutherland P.G., Weisskopf M.G., Kahn S.M., 1978, *ApJ*, 219, 1024

Szatmary K., Vinko J., Gal J., 1994, *A&AS*, 108, 377

Terrell N.J. Jr., 1972, *ApJ*, 174, L35

Torrence C., Compo G.P., 1998, *BAMS*, 79, 61

Uttley P., McHardy I.M. 2001, *MNRAS*, 323, L26

Uttley P., 2004, *MNRAS*, 347, L61

Vaughan S., Edelson R., Warwick R.S., Uttley P., 2003, *MNRAS*, 345, 1271

Walborn N., 1973, *ApJ*, 179, L123

Webster B.L., Murdin P., 1972, *Nature*, 235, 37

Wilms J., Nowak M.A., Pottschmidt K., Heindl W.A., Dove J.B., Begelman M.C., 2001, *MNRAS*, 320, 327

Zdziarski A.A. et al., 2004, *MNRAS*, 351, 791

Zhang W., Jahoda K., Swank J.H., Morgan E.H., Giles A.B., 1995, ApJ, 449, 930  
 Ziolkowski J., 2004, MNRAS, submitted  
 Źycki P.T., 2002, MNRAS, 333, 800  
 Źycki P.T., 2003, MNRAS, 340, 639

## APPENDIX A: DISCRETE FORM OF CWT IN TERMS OF FOURIER TRANSFORM

Let us express a continuous wavelet transform (16) as the convolution of Fourier transforms of the lightcurve and wavelet function in the following way:

$$w_{a,b} = \int_{-\infty}^{\infty} \hat{x}(\nu) \hat{\psi}_{a,b}^*(\nu) d\nu. \quad (\text{A1})$$

The Fourier transform of  $\psi_{a,b}$  is given by:

$$\hat{\psi}_{a,b}(\nu) = \frac{1}{\sqrt{a}} \int_{-\infty}^{\infty} \psi\left(\frac{t-b}{a}\right) e^{-i2\pi\nu t} dt. \quad (\text{A2})$$

Substituting  $(t-b)/a$  by  $\eta$  equation (A2) evaluates into:

$$\hat{\psi}_{a,b}(\nu) = \sqrt{a} e^{-i2\pi\nu b} \int_{-\infty}^{\infty} \psi(\eta) e^{-i2\pi a\nu \eta} d\eta \quad (\text{A3})$$

where a constant component was separated out. As one can see, an integral expression can be considered as the Fourier transform of a wavelet function where  $2\pi a\nu$  is a rescaled angular frequency. Thus it is possible to denote (A3) shortly:

$$\hat{\psi}_{a,b}(\nu) = \sqrt{2\pi a} e^{-i2\pi\nu b} \hat{\psi}(2\pi a\nu) \quad (\text{A4})$$

and therefore a CWT as the inverse Fourier transform of the product:

$$w_{a,b} = \sqrt{2\pi a} \int_{-\infty}^{\infty} \hat{x}(\nu) \hat{\psi}^*(2\pi a\nu) e^{i2\pi\nu b} d\nu \quad (\text{A5})$$

where complex conjugate of the Fourier transform of  $\psi$  function was taken into account.

A discrete Fourier transform of  $x_k$  is given by equation (3) where  $j$  denotes a frequency index. Performing discrete notation of time-shifting factor as  $b = k\Delta t$  where  $\Delta t$  stands for sampling time of a lightcurve, one can write down a *discrete form of continuous wavelet transform in terms of Fourier transform* as:

$$w_k(a) = \left(\frac{2\pi a}{\Delta t}\right)^{1/2} \sum_{j=1}^{N_{\text{obs}}} \hat{x}_j \hat{\psi}^*(2\pi a\nu_j) e^{i2\pi\nu_j k\Delta t} \quad (\text{A6})$$

where frequency  $\nu_j$  equals:

$$\nu_j = \begin{cases} j/(N_{\text{obs}}\Delta t) & \text{for } j \leq N_{\text{obs}}/2 \\ -j/(N_{\text{obs}}\Delta t) & \text{for } j > N_{\text{obs}}/2 \end{cases} \quad (\text{A7})$$

and the factor  $(2\pi a/\Delta t)^{1/2}$  ensures that wavelet will keep the same energy at every scale  $a$ . Because of finite duration of the signal, the proper choice of scales must be done. The largest scale would correspond to the lightcurve span of  $T$  whereas the smallest one ought to be an equivalent of Fourier Nyquist frequency, i.e.  $a_0 = 2\Delta t$ . In fact, the selection of scales in this region can be chosen arbitrarily with step in scale not smaller than  $a_0$ . However, in case of very fine signal when a few decades of scales is wished to be covered, one can build the wavelet transform choosing:

$$a_m = a_0 2^{m\Delta m} \quad m = 0, \dots, M \quad (\text{A8})$$

where

$$M = \Delta m^{-1} \log_2(N_{\text{obs}} \Delta t a_0^{-1}) \quad (\text{A9})$$

(TC98) and thus rewriting (A6) in the following way:

$$w_k(a_m) = \left(\frac{2\pi a_m}{\Delta t}\right)^{1/2} \sum_{j=1}^{N_{\text{obs}}} \hat{x}_j \hat{\psi}^*(2\pi a_m \nu_j) e^{i2\pi\nu_j k\Delta t}. \quad (\text{A10})$$

This paper has been typeset from a  $\text{\TeX}$ /  $\text{\LaTeX}$  file prepared by the author.